INORGANIC CHEMISTRY
FRONTIERS

CHINESE CHEMICAL SOCIETY

ROYAL SOCIETY OF CHEMISTRY

RESEARCH ARTICLE

View Article Online
View Journal | View Issue

Cite this: *Inorg. Chem. Front.*, 2023, **10**, 3686

Mechanism of action of an Ir(III) complex bearing a boronic acid active as a H_2O_2-responsive photosensitizer: ROS generation and quinone methide release for GSH scavenging†

Pierraffaele Barretta and Gloria Mazzone *

A DFT-based theoretical investigation is reported here to clarify the mechanism of action of a recently synthesized Ir(III) complex, **Ir-B(OH)$_2$**, characterized by the presence of an aryl boronic acid moiety on one bidentate ligand that can detect H_2O_2 in cancer cells. The H_2O_2-mediated oxidation of boronic acids under physiological conditions affords the active complex for PDT application, **Ir-OH**, and a quinone methide (QM) as a by-product, which in turn can scavenge glutathione (GSH) compromising one of the most powerful cellular defence against the ROS produced by PDT treatments. The most plausible reaction mechanism for the oxidation of the aryl boronic acid by H_2O_2 is described. The formation of the products, namely the PS **Ir-OH** and the QM, is achieved overcoming an energy barrier of 33 kcal mol^{-1} and with a considerable energy gain. The description of the subsequent GSH scavenging mechanism by the released QM evidences that the reaction occurs with a low energy expense. Moreover, the computation of the photophysical properties, needed for evaluating the occurrence of type I and type II processes, of the prodrug **Ir-B(OH)$_2$** and the active PS **Ir-OH** suggests that they are both able to generate the singlet molecular oxygen, $^1O_2$, while other ROS cannot be achieved. Moreover, the MOs involved in the excited states population, both singlet and triplet, unravel the key role of the metal centre in the ISC process.

Received 1st February 2023,
Accepted 12th May 2023

DOI: 10.1039/d3qi00203a

rsc.li/frontiers-inorganic

Introduction

Photodynamic therapy (PDT) is a clinical non-invasive methodology for the treatment of certain diseases including cancer.[1,2] It is based on the injection of a photosensitizer (PS) into the body; diffusion of the PS; and activation of the PS with specific electromagnetic waves, which belong to the therapeutic window (600–850 nm): they are absorbed by the PS and promote electronic transitions from the ground state (S_0) of the PS to excited ones (S_m); the excited states produced transition, through non-radiative intersystem crossing (ISC), to triplet excited states (T_n), which are characterized by a longer life time. The triplet excited states are then deactivated according to two different mechanisms in presence of molecular oxygen and are responsible for cytotoxic species generation. The so-called type I process produces reactive oxygen species (ROS) by electron or hydrogen transfer, while the type II reaction generates singlet oxygen ($^1O_2$) by energy transfer. ROS and $^1O_2$ induce oxidative stress and apoptosis in cells destroying diseased tissues.[3–5] The great advantage of PDT is the time and space control of drug activation. In fact, a good PS has to be non-toxic in the dark and activated only upon irradiation with light. This reduces the side effects, limiting the range of action to diseased and surrounding tissues. Nevertheless, several efforts have been devoted to enhance the therapeutic efficiency by designing PSs that accumulate selectively in a specific cell organelle. Mitochondria represent one of the most desired targets as they play a pivotal role in a variety of cellular processes, such as cell death regulation and redox signalling.[6,7]

Department of Chemistry and Chemical Technologies, University of Calabria, 87036 Rende, CS, Italy. E-mail: gloria.mazzone@unical.it

† Electronic supplementary information (ESI) available: Optimized structures of the minima intercepted along both neutral and anion pathways; free energy profiles in water describing GSH alkylation by the QM computed at the B3LYP/6-31G** level of theory; intrinsic reaction coordinate calculation of TS″ in the forward direction leading to product formation; benchmark of exchange and correlation functional and basis set on the maximum absorption wavelength in water for **Ir-OH** and discussion; TDDFT outcomes for **Ir-B(OH)$_2$** and **Ir-OH**; computed UV–Vis spectra; lowest triplet state excitation energies for the investigated Ir(III) complexes; NTOs of bright and triplet states computed for **Ir-B(OH)$_2$**; Cartesian coordinates of all the minima and transition states located along the free energy profiles describing the H_2O_2-mediated oxidation of aryl boronic acid and GSH scavenging by the QM, as well as those of the Ir(III) complexes whose photophysical properties have been described. See DOI: **https://doi.org/10.1039/d3qi00203a**

Moreover, cancer cells exhibit various alterations to mitochondrial functions which can be exploited to target cancer cells for a selective therapeutic response.[8,9]

In recent years, the development of multi-action antitumor compounds oriented toward different biological targets or based on synergistically combined antitumor effects has taken hold. Transition metal complexes, especially of Ru^{2+}, Ir^{3+}, Pt^{2+}, Pt^{4+}, Rh^{3+} and Os^{2+}, are promising PSs for this purpose, thanks to their photostability, biocompatibility, high absorption within the therapeutic window, high triplet state quantum yield, and high quantum yield of $^1O_2$ and the possibility to bind target agents for increasing the selectivity.[10–20] In addition, the presence of the metal centre promotes spin–orbit coupling (SOC) and in turn an efficient ISC, giving access to multiple long-lived excited states, inaccessible to organic chromophores. Among the metal-containing PSs, cyclometalated Ir(III) complexes occupy a prominent place since they possess a series of advantageous properties for biological applications.[21] Different organelle-targeted Ir(III) complexes have been synthesized and proposed as PSs in PDT under normoxic and hypoxic conditions, such as complexes containing cationic triphenyl phosphines or a triphenylsulfonium salt that target mitochondria[22,23] or others that localize in lysosomes.[24] Nevertheless, whatever the target, the generated ROS with the PDT treatment could be neutralized by the defence mechanisms present in cancer cells, which are already under oxidative stress associated with oncogenic transformation and alteration in metabolic activity.[25–28] Under these conditions, cells are able to adapt to survive owing to the redox buffering system and various antioxidant enzymes. The glutathione system (GSSG/2GSH) is the most abundant redox couple in maintaining cellular redox balance;[29] therefore, the presence of GSH in cancer cells can reduce the effect of PDT.[30,31] Among the ROS present in a high level in cancer cells, in contrast to the healthy ones, hydrogen peroxide (H_2O_2) is one of the most abundant and could be utilized as a target agent.[32] For instance, aryl boronic acids and their esters are used as H_2O_2-responsive moieties owing to the ease of synthesis and good biocompatibility as the products of the reaction show no cytotoxicity and the reaction with H_2O_2 is highly selective.[33–36] These prodrugs are designed to release quinone methide (QM) as a by-product,[30,32,37,38] which was reported to rapidly alkylate GSH, leaving cells defenceless from ROS,[38,39] thus allowing an enhancement of PDT efficacy.

Liao *et al.*[37] reported the rational design of a mitochondria-targeting iridium-based prodrug for two-photon PDT. The PS is composed of a cyclometalated Ir(III) complex, named **IrB(OH)$_2$** (Scheme 1), with a ligand bearing a moiety that, thanks to the presence of a boronic acid on one extremity, can release the QM upon reaction with H_2O_2. They found that in the presence of H_2O_2 the equally PDT-active complex, named **Ir-OH**, is formed and that the concomitant QM release amplifies its PDT action.

Despite several works reporting the H_2O_2-mediated oxidation of boronic acids under physiological conditions,[36,40,41] only some propose a detailed reaction mechanism for the attack of H_2O_2 on such systems. The aim of the present work is two-fold. On the one hand, we have searched for the most plausible reaction mechanism for the oxidation of the aryl boronic acid moiety, the H_2O_2-responsive part of the prodrug **Ir-B(OH)$_2$**,[37] that allows the release of the GSH scavenger QM and the PS **Ir-OH**. On the other hand, the photophysical properties of both the prodrug and the generated PS **Ir-OH**, upon H_2O_2-mediated oxidation, have been explored for unravelling the key characteristics for PDT application.

In addition, as underlined by the authors, the whole action of the **Ir-B(OH)$_2$** prodrug should include the QM scavenging action against GSH. They have investigated the release and the ability to reduce GSH depending on the concentration of the drug, observing that the levels of GSH are reduced by about 20% by **Ir-B(OH)$_2$** in the dark at a concentration of 2 μM.[37] Therefore, as the QM would add extra action to the prodrug, the energies involved for its GSH scavenging action have been determined. Density functional theory and its time-dependent formulation (TD-DFT) have been used for this purpose.

Results and discussion

Reaction mechanism for oxidation of boronic acid by H_2O_2

The mechanism of action of **Ir-B(OH)$_2$** starts with the reaction of the boronic acid group, present on one extremity of the complex, with H_2O_2.[37] The detailed reaction mechanism for H_2O_2-mediated oxidation of boronic acids in physiological conditions is still debated.[36,40,41] Some studies report the H_2O_2-triggered oxidation of boronic acid hypothesizing the primary deprotonation of H_2O_2 to yield HOO^- anion, which is, thus, the species appointed for the nucleophilic addition to the

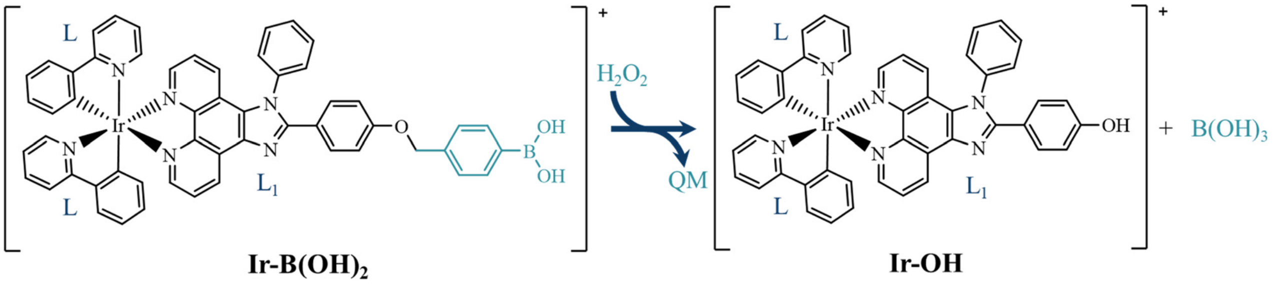

Scheme 1 Structures of complexes **Ir-B(OH)$_2$** and **Ir-OH**.

boron atom.[36,40] For exploring the reaction mechanism of the H_2O_2-triggered oxidation of boronic acid present on one extremity of the **Ir-B(OH)$_2$** complex, the neutral H_2O_2 molecule and the anion HOO^- have been, then, considered along with the sole portion of the complex that effectively takes part in the reaction with H_2O_2, that is the aryl boronic acid. At the end of the whole process, the QM and the active PS **Ir-OH** complex are released.

To properly simulate the physiological environment, all the calculations have been carried out in implicit water medium. In addition, six explicit water molecules have been included for better simulating the microsolvation around the key portion of the system and to assist the whole process. Indeed, some water molecules directly participate in the reaction while others simply stabilize the system by establishing a network of hydrogen bonds.

Fig. 1 shows the free energy profiles for the whole reaction when the two species are independently involved in the process, named neutral (blue line) and anion (red line) pathways if H_2O_2 or HOO^- are involved in the reaction. All the relative energies have been calculated with respect to the first adduct generated by the primary interaction between the aryl boronic acid (4-(phenoxymethyl)phenyl)boronic acid) and hydrogen peroxide, neutral (ADD1) or anion (ADD2), properly surrounded by a critical number of water molecules. Fig. 2 shows the optimized structures of the transition states (TSs) sketched in Fig. 1, while all the minima are reported in Fig. S1 of the ESI.† In such representations, only the atoms directly involved and water molecules taking part in each step of the reaction mechanism are drawn in a ball and stick representation and individually labelled, while all the other atoms are represented in lines.

Along the neutral pathway, Fig. 1a, once the initial reactant interaction in ADD1 has occurred, the process starts with the H_2O_2 nucleophile attacking the boron atom, which is realized by overcoming an energy barrier of 33.3 kcal mol^{-1} (TS1). In the located TS, a hydrogen atom transfer from O1 to O2 occurs, as evidenced by the associated imaginary vibrational frequency. In the formed hydroperoxide intermediate, INT1, the boron atom returns into a trigonal arrangement and a water molecule is released. The intercepted stationary point lies 2.7 kcal mol^{-1} below the reference adduct, resulting in a weakly exergonic process. At this point, a water molecule, here considered as the one released in the first step, attacks the boron atom in the second part of the reaction to afford the tetrahedral intermediate, INT2, which is formed with an energy expense of 7.3 kcal mol^{-1}. The formation of the new bond B–O2 is endergonic (by 4.9 kcal mol^{-1}). However, overall, the tetrahedral intermediate formation, occurring in the two steps just described, is approximately thermo-neutral with respect to the first adduct (2.2 kcal mol^{-1}). Looking at the mechanism found for the attack of the anion species on the boron atom (Fig. 1b), it can be seen that the tetrahedral intermediate formation, with the restoring of the B–O1 bond (Fig. 2b), occurs in one step with a considerably less energy expense (9.3 kcal mol^{-1}) for the reaction to take place. The product of TS7, INT6, is accomplished with a slight energy gain (1.2 kcal mol^{-1}).

The third step of the neutral pathway provides a hydrogen atom transfer from O2 to O3. The imaginary frequency found in the associated TS3 indicates a typical Grotthuss mechanism:[42] a very fast proton transfer from a water molecule to another, by the cooperative formation and breaking of hydrogen bonds that connect the same water molecules. In this way, two water molecules are involved in the transfer of a proton from O2 to O3 as can be seen in the optimized structure of TS3. For such a step to occur, 11.2 kcal mol^{-1} is required. The formation of INT3 is endergonic by about 8 kcal mol^{-1}. The subsequent step 4 is realized through TS4 with an energy expense of 10.2 kcal mol^{-1}. The imaginary frequency associated with this TS evidences the insertion of O1 into the B–C1 bond and the simultaneous breaking of the O1–O6 bond along with the elimination of a water molecule. Such a concerted movement affords the formation of intermediate INT4, which is highly stabilized with respect to the transition state leading to it. This energy gain is probably due to the restoring of the boron atom hybridization in a trigonal arrangement thanks to the formation of the B–O1 bond and to the presence of three oxygen atoms around the boron atom that transfer more charge density to the electron-deficient centre with respect to the old configuration, INT3, where the boron atom is bonded to two oxygen atoms and a carbon atom. Again, the anion pathway differs in the number of steps required for the trigonal structure restoration because it occurs in a single step where the insertion of oxygen O1 into the B–C1 bond requires only 9 kcal mol^{-1} (TS8) to be realized. The formed intermediate INT7 presents the great stabilization already observed along the neutral pathway.

From here, the reaction proceeds with the release of $B(OH)_3$. While along the neutral pathway such a release occurs in one step, in the anion process it is a two-step mechanism. Following the former pathway, from INT4, in which the water molecule eliminated in the previous step is already prone to approach the boron atom, the nuclophile attack is realized through the TS5, which entails the loss of the boron trigonal geometry for the B-O6 bond to be formed. The computed imaginary frequency indicates the transfer of a proton from O6 to O1 and the simultaneous breaking of the B–O1 bond, with the definitive elimination of boric acid ($B(OH)_3$). Such an attack requires 23.9 kcal mol^{-1} to take place and the formed intermediate INT5 is stabilized by about 8.0 kcal mol^{-1} with respect to the preceding minimum, owing to the restored trigonal geometry around the boron atom in the elimination of boric acid. Along the anion pathway, the HO^- attack on the boron atom and the release of $B(OH)_3$ occur according to a stepwise mechanism. However, the attack of a charged species (HO^-) on the boron atom, realized through TS9, costs much less energy, similarly to what has been observed in the primary attack of HOO^- on the boron atom (TS7). Indeed, the overcoming of low energy barriers (3.0 and 13.3 kcal mol^{-1} for the two steps, respectively) is accomplished to afford first the tetrahedral intermediate INT8 and then the final INT9.

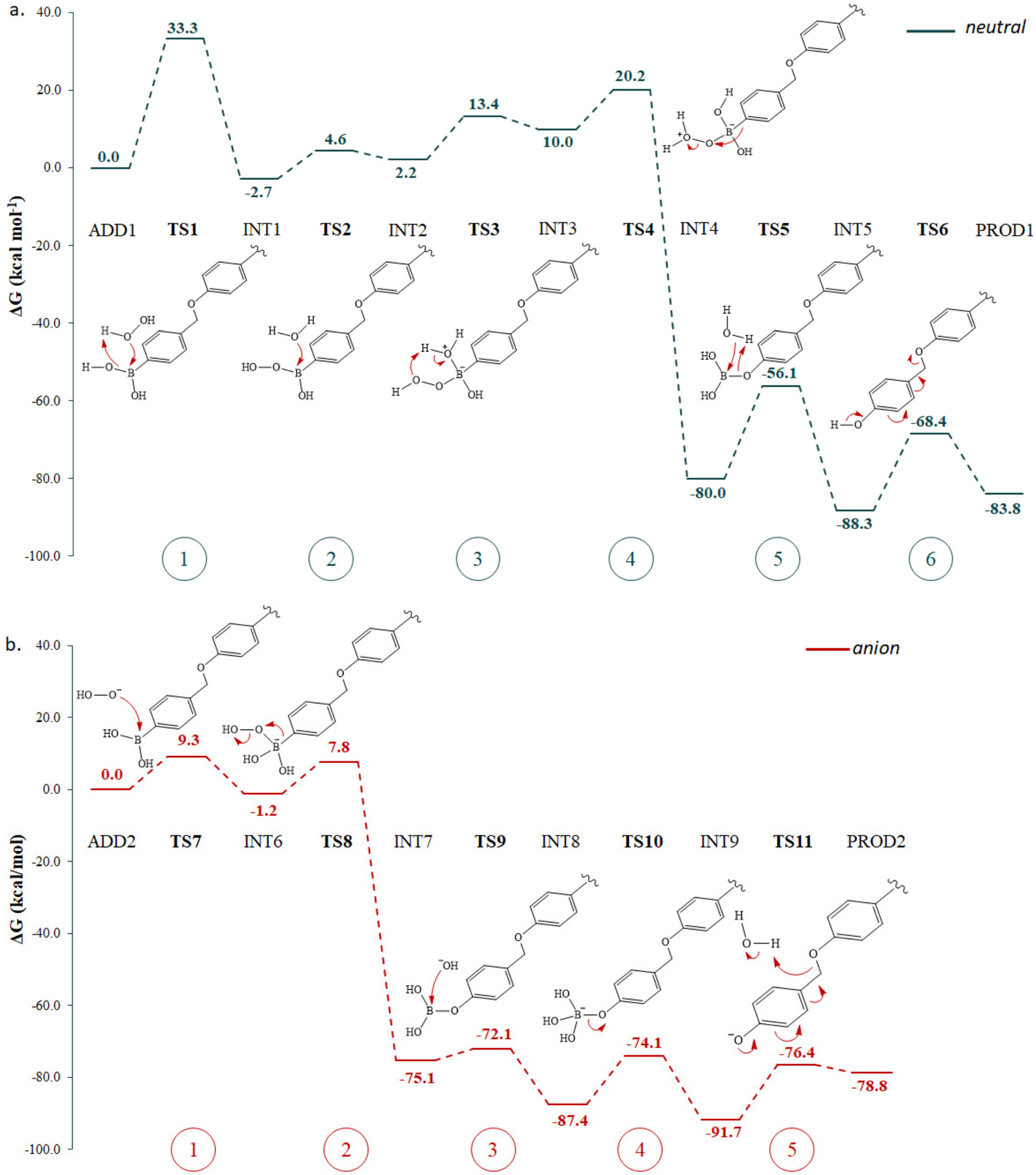

Fig. 1 Free energy profiles in water describing (a) H_2O_2- and (b) HOO^--mediated oxidation of aryl boronic acid to release QM. A sketch of the intercepted TSs are also reported.

The last step serves to form the QM and release the PS. Again, in the two explored mechanisms, different interactions favour QM formation. Along the neutral pathway, a network of H-bonds assists the transfer of the proton from O1 to O7. The proton transfer is realized with the same Grotthuss mechanism seen in TS3: in this case (TS6), three water molecules are involved, connected by a network of H-bonds. The anion pathway, instead, involves just the reactant water molecule for the proton transfer from water oxygen O3 to O7. This process requires 19.9 kcal mol^{-1} and 15.3 kcal mol^{-1} to be realized along the neutral and anion pathways, respectively. It entails the loss of aromaticity of the ring in favour of double bond for-

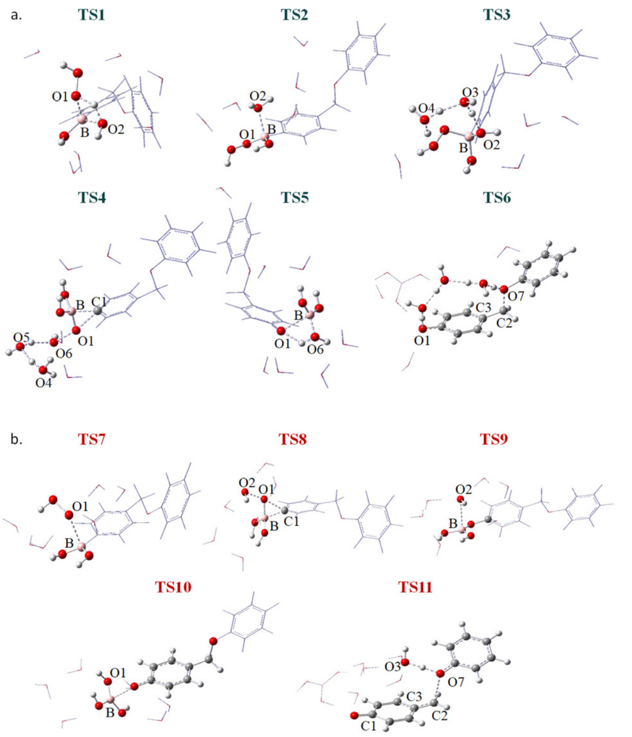

Fig. 2 Optimized structures of TSs located along the free energy profiles reported in Fig. 1 for (a) H_2O_2 and (b) HOO^- attacks, respectively.

mation between O1 and C1 and between C2 and C3. Thus, on the basis of the model used for the calculations, QM formation is accompanied by phenol release, which, in the real model, corresponds to the active PS **Ir-OH**. This final step is endergonic in both cases, the final product being destabilized by 4.5 and 12.9 kcal mol^{-1} compared to the starting adduct of this step, INT5 and INT9 for neutral and anion pathways, respectively. However, despite the endergonicity of a few steps along the intercepted pathways, the overall release of the GSH scavenger QM and the PS **Ir-OH** is powerfully favoured from a thermodynamic point view and entails an energy gain of around 80.0 kcal mol^{-1} following both the pathways. The energies involved in the two explored pathways are, instead, significantly different from a kinetic point of view. Indeed, while the first step, which corresponds to the hydroperoxide attack on the boron atom, requires the highest amount of energy (activation energy of 33.3 kcal mol^{-1}) along the neutral pathway, the rate-determining step (RDS) of the whole oxidation reaction within the anion process is represented by the cleavage of the C2–O7 bond in favour of QM release. However, all the steps occur easily if HOO^- is the reactant species of H_2O_2.

Moreover, it is worth noting that, in the biological environment, the tunnelling effect, in the reaction steps involving H-transfer, can further facilitate the whole reaction. As such a transfer is involved in the RDS of both the reaction mechanisms investigated here, it has been estimated and it has been found that it could enhance the reaction rate up to one order of magnitude.

Mechanism of GSH scavenging by QM

As soft electrophiles, quinones are particularly susceptible to GSH conjugation reactions, and usually, the reaction is so easy that enzymatic catalysts (such as glutathione *S*-transferase) are not needed. This attribute has been exploited by Liao *et al.*[37] for the synergistic anticancer effects from sequential actions of GSH-scavenging QM and photo-induced ROS generating **Ir-OH** complex, whose properties will be discussed in the next section. All the effects are mediated by the action of H_2O_2 present in excess in cancer cells, which are essential for yielding the active species, as described above.

In order to provide a complete description of the H_2O_2-triggered anticancer action, the inhibition of antioxidant GSH exerted by the QM released after PS generation has been explored at the same level of theory described above, including the microsolvation environment provided by six water molecules. At physiological pH, GSH exists in its zwitterionic form at the glutamyl residue, the side-chain of the cysteine bears a neutral thiol (SH) unit and the carboxyl group of glycine is deprotonated. As the main part of the reductant involved in the process is represented by the SH extremity, the glutamyl residue has been removed, as previously considered.[43]

The GSH reaction with quinone rings usually occurs *via* a Michael addition forming the corresponding hydroquinones.[44,45] In the case of the QM here examined, the reaction should entail the H transfer from the SH group of GSH to the carbonyl oxygen atom of the QM and the concomitant alkylation of glutathione by forming a phenol–SG adduct. To the best of our knowledge, no detailed information about the energetics of the process is available. Preliminary calculations with a leaner protocol (Fig. S2†) evidenced that the reaction occurs in a concerted manner according to which the S–C2 bond formation is realized at the same time as the H transfer to the O1 atom of the QM to afford the phenol–SG adduct. The intervention of an increasing number of water molecules has been considered to detect the most probable reaction mechanism. The outcomes of such exploration evidenced that at least three water molecules are required to assist the H transfer from GSH to the QM. In Scheme 2, the found reaction mechanism has been depicted.

In Fig. 3, instead, the free energy profile obtained by applying the same protocol used for the previous calculations has been shown, which describes both oxygen and sulphur atoms

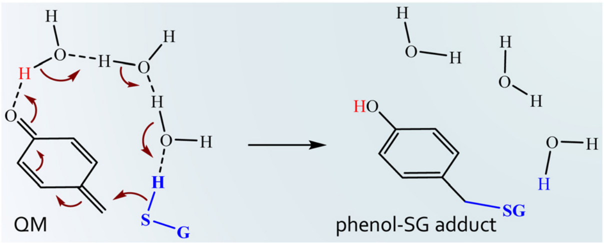

Scheme 2 Reaction mechanism for H-transfer from GSH to the QM and concomitant GSH alkylation to afford phenol–SG adduct formation.

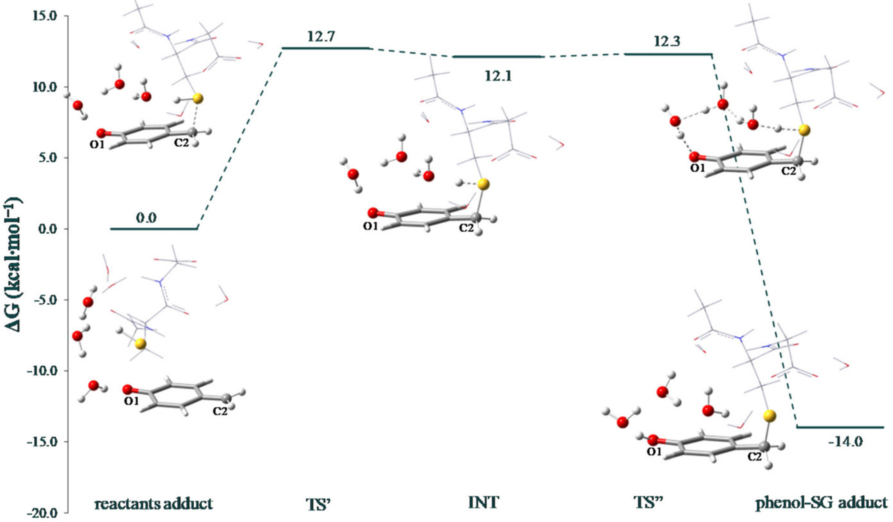

Fig. 3 Free energy profiles in water describing the GSH alkylation with the QM. The optimized structures for each stationary point are also provided.

by adding a diffuse function on their basis set. The relative energies have been calculated with respect to the initial reactant adduct that includes the QM, GSH and six water molecules. At first glance it can be noted that, differently from preliminary calculations, the reaction occurs according to a pseudo two-step mechanism, according to which the first part provides the formation of an unstable intermediate (labelled INT) that rapidly evolves to the final product in the second step. However, comparing the outcomes reported in Fig. S2† and Fig. 3, it can be seen that the energies involved are essentially the same, from both kinetic and thermodynamic points of view.

In all the located stationary points before product formation, some water molecules serve as a proton shuttle from GSH to the QM, as they establish a network of H-bonds between the hydrogen of the SH group and the carbonyl oxygen O1 of the QM. In the first transition state TS′ the imaginary frequency is associated only with the C–S bond stretching ($i184\ \text{cm}^{-1}$), indicating that the C2–S bond is formed before a complete H transfer, although a slight elongation of the S–H bond can be previously observed in the TS′.

Indeed, the S–H bond from 1.353 Å in the reactant adduct increases to 1.379 Å in TS′ and 1.409 Å in the resulted INT. INT is, thus, characterized by tetrahedralization of the C2 atom and the shortening of the S–C2 distance, which from 2.175 in the TS′ becomes 1.941 Å in INT. The energy barrier to be overcome for S–C2 bond formation is found to be 12.7 kcal mol^{-1} and the resulted INT is stabilized by only 0.6 kcal mol^{-1} than the transition state leading to it. In the second transition state TS″, an elongation of the C═O bond and a further shortening of the S–C2 distance (1.912 Å) can be observed. The computed imaginary frequency ($i435\ \text{cm}^{-1}$) clearly reveals the H transfer from S to the vicinal water molecule oxygen and the S–H distance becomes 1.527 Å. The inspection of IRC calculation shows that the H transfer to the nearest oxygen is followed by the transfer to the oxygen atoms in subsequent water molecules up to the carbonyl O2 to afford the final product (see Fig. S3†). Such a TS lies only 0.2 kcal mol^{-1} above the energy of the minimum proceeding it.

Thus, it can be argued that the second step is effectively barrierless and that the whole reaction occurs overcoming the first energy barrier of 12.7 kcal mol^{-1}. The formation of the phenol–SG adduct is accomplished with an energy gain of 14.0 kcal mol^{-1}. Thus, the whole reaction being exergonic, the GSH scavenging by the QM is favoured from both kinetic and thermodynamic points of view. Furthermore, the energetics found is consistent with the evidence that the electrophilic QM rapidly reacts with nucleophilic GSH,[46,47] thus enhancing the PDT efficacy.

On the basis of these findings, the limited reduction of GSH level (less than 20%) can be ascribed to the imbalance between the complex and GSH concentrations.[37] As is known, GSH is present in mM concentration within cells; hence a concentration of 2 μM of the complex could limit its action as a GSH scavenger.

Absorption spectra of Ir(III) complexes

The computational evaluation of the photophysical properties is somewhat difficult with cost-effective protocols. However, TD-DFT represents a good balance between accuracy and computational cost[48] and it has been provided that hybrid functionals are able to properly locate and characterize the absorption bands. However, to describe the photophysical features of the complexes under examination as well as the main parameters for evaluating their photodynamic action, a preliminary benchmark has been carried out on the maximum absorption wavelength $\lambda_{\max}$, for the effective PS **Ir-OH**, in order to select the most suitable protocol (see Table S1† and related discussion). From our exploration the hybrid PBE0 emerged as the best choice. A further benchmarking on the size of the used basis sets (Table S2†) has evidenced that the 6-311G(d,p) basis set is the most suitable in reproducing such a parameter. PBE0 coupled with the 6-311G(d,p) basis set has been, thus, used for all the TD-DFT simulations, including triplet states' energy and spin–orbit matrix elements. The absorption spectra have been computed in the implicit water solvent in order to mimic as best as possible the phosphate buffered saline (PBS) experimental medium.[37] The outcomes, namely excitation energies, absorption wavelengths, oscillator strength and molecular orbital contribution to each transition, have been listed in Table S3,† along with the character assignment to each electronic transition on the basis of the analysis of the natural transition orbitals (NTOs). The simulated spectra, shown in Fig. S4,† confirm the presence of a main absorption band in the 250–600 nm region for both the investigated complexes. It is centred at around 270 nm and presents a shoulder at approximately 430 nm, in good agreement with the experimental evidence.[37] However, some singlet states present a different characteristic, *e.g.* the excited state with the highest oscillator strength (around 260 nm) evidently showing a contribution of IL_1CT together with the ML_1CT: in this case the only ligand involved in the CT is that named L_1 in Scheme 1. Although the lowest-frequency transition mainly originates from an electron promotion from the HOMO to the LUMO, the other transitions mostly start from inner orbitals (*e.g.* H-7, H-9) and end at outer ones (*e.g.* L+2, L+5). In addition, differently from the generation of the first excited singlet state that is almost a pure H → L transition, the other excited states originate even by an equal contribution of a few electronic transitions (see *e.g.* the excited state at around 290 nm in Table S2†). No significant differences, perhaps a few nanometres on a few transitions, have been found for the two complexes, the prodrug **Ir-B(OH)$_2$** and the active PS **Ir-OH**. The very similar behavior evidences the maintenance of the photophysical properties of the iridium complex upon B–C bond cleavage.

Photodynamic processes

Once the complex is excited and then a singlet excited state populated, the photodynamic action requires other processes to be triggered: (i) the ISC radiationless transition from a singlet state, usually the bright one, to a long-lived triplet state with lower energy; and (ii) the subsequent deactivation of the triplet state following type I or type II photoreactions, both of which lead to ROS formation. The former process involves the generation of radical ions and free radicals, together with the generation of the superoxide anion $O_2^{-\bullet}$, whose fast bimolecular decay leads to the production of other highly oxidizing and reactive species (such as hydroperoxyl radicals $HO_2^{\bullet}$) able to react with several biomolecules irreversibly degrading them. The type II reactions, instead, entail the transfer of the triplet state energy to molecular oxygen to produce one of the most harmful ROS, the cytotoxic agent $^1O_2$. The occurring of the first part of the photodynamic action, that is the triplet state population by ISC, can be evaluated by taking into consideration Fermi's golden rule for the ISC rate of deactivation channels of the bright S_1 state, according to which the kinetics mainly depend on spin–orbit matrix elements and the energy splitting between the coupled state:

$$k_{\mathrm{ISC}} \propto \frac{\left\langle \Psi_{\mathrm{S}_1} \middle| \widehat{H_{\mathrm{SO}}} \middle| \Psi_{\mathrm{T}_n}{}^2 \right\rangle}{\Delta E_{\mathrm{S}_1-\mathrm{T}_n}} \quad (1)$$

where $\hat{H}_{\mathrm{SO}}$ is the spin–orbit Hamiltonian, $\Delta E_{\mathrm{S}_1\text{–}\mathrm{T}_n}$ is the S_1–T_n energy gap; $<\Psi_{\mathrm{S}_1}|\hat{H}_{\mathrm{SO}}|\Psi_{\mathrm{T}_n}>$ is the spin–orbit matrix element between the initial (S_1) and the final (T_n, with n = 1–5) wavefunction. These parameters have been determined for both the studied complexes **Ir-B(OH)$_2$** and **Ir-OH**[37] and are listed in Table 1, where SOCs have been calculated according to eqn (2) defined in the computational details section. The complexes present a series of five triplet states with suitable energies to couple with the singlet bright one (see Table S4†). The computed SOCs evidence that all the radiationless transitions starting from S_1 could be in principle very fast, as more than 100 cm^{-1} have been obtained for almost all the possible deactivation channels. The high couplings found can be rationalized looking at the different nature of the coupled states, determined on the basis of the NTOs shown in Fig. 4 and Fig. S5† for **Ir-OH** and **Ir-B(OH)$_2$**, respectively, along with the evident participation of the metal in most of the involved NTOs of each state, both singlet and triplet ones.

The triplet states lying below, though originating from more than one transition (see Table S4†), can be considered essentially of the type ILCT. The triplet states T_1 and T_2 are mainly centred on the L_1 ligand and are thus labelled as IL_1CT; although T_3 and T_5 are centred on the two ppy ligands (ILCT), respectively, in T_4 a charge transfer from a ppy ligand to the L_1 occurs (LL_1CT). Looking at all the NTOs reported, a participation of the metal in the charge density of holes and, to some extent, also of particles can be observed. Indeed, analysing the composition of the molecular orbitals constituting the NTO plots, there is a participation of the metal in most of them, thus, a contribution of MLCT is present in all the triplet states. Therefore, there are five deactivation channels than could be in principle followed for a triplet state population. However, considering the other parameter that contributes to the ISC efficiency, the singlet–triplet energy splitting, some singlet state deactivation channels could be less favourable than others; see *e.g.* the energy gap between S_1 and T_1 that is

Table 1 Spin–orbit matrix elements (SOC, cm^{-1}) and energy splitting (ΔE, eV) between singlet S_1 and triplet T_n excited states computed for the investigated Ir(III) complexes

	Ir-B(OH)$_2$		**Ir-OH**	
Channel	SOC	ΔE	SOC	ΔE
$S_1 \rightarrow T_1$	170.2	0.27	180.2	0.27
$S_1 \rightarrow T_2$	694.7	0.23	691.3	0.23
$S_1 \rightarrow T_3$	1061.6	0.09	1062.6	0.09
$S_1 \rightarrow T_4$	114.6	0.03	119.6	0.03
$S_1 \rightarrow T_5$	66.4	0.02	46.7	0.02

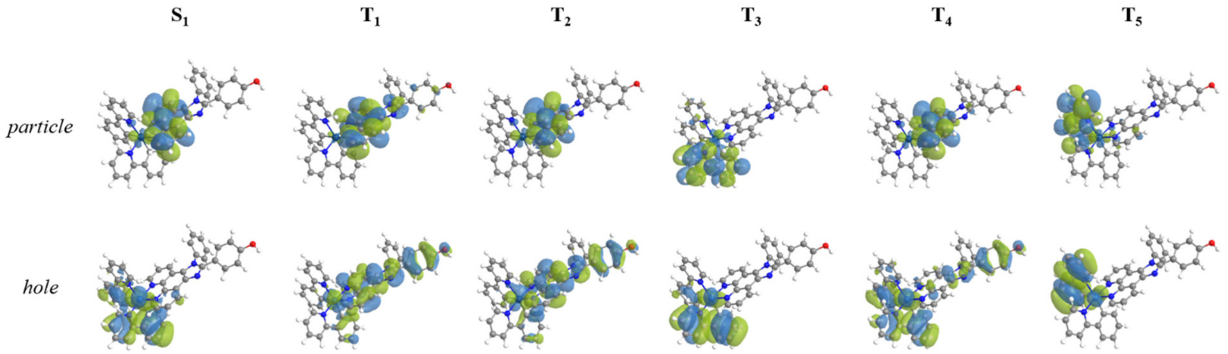

Fig. 4 NTOs of bright and triplet states computed for **Ir-OH**. Green and light blue colors stand for gained and lost electron density, respectively. NTO plots are generated using Chemissian software v4.67.[53]

one order of magnitude greater than that for S_1–T_4. Combining the two parameters on which ISC depends, the coupling between S_1 and T_3 should be the most probable one and it is promoted by a high SOC value and occurs between states separated by a relatively small gap (0.09 eV).

For type II reactions to occur, once a triplet state is populated, it is essential that it has enough energy to promote the excitation of molecular oxygen in order to produce the cytotoxic agent for PDT, that is singlet oxygen.

The triplet-singlet energy gap of O_2 has been previously determined employing different combination of functionals and basis sets,[49–52] in particular at the PBE0/SDD/6-31+G** level an energy splitting of 0.93 eV has been computed in good agreement with the experimental value of 0.98 eV. Thus, the triplet of the Ir(III) complex involved in the energy transfer to molecular oxygen should lie at least 0.93 eV above its ground state. Also considering the occurrence of an internal conversion from the T_3 state to populate the low-lying triplet state, T_1, both the prodrug **Ir-B(OH)$_2$** and the active PS **Ir-OH** can promote molecular oxygen excitation according to type II photoreactions, as T_1 state lies at 2.59 eV. However, once the triplet state is populated also type I pathways can be triggered that ultimately lead to $O_2^{-\bullet}$ production. In such processes, the PS in the triplet state can directly interact with molecular oxygen to transfer an electron or be involved in autoionization reactions, according to which the reduction of the triplet state is operated by the PS in its ground (pathway a) or triplet state (pathway b), before the interaction with molecular oxygen.

The autoionization reactions can be schematized as follows, in which the PS in the ground state is generally indicated as $[\mathrm{Ir}]^+$:

$$\text{a. } {}^3[\mathrm{Ir}]^+ + [\mathrm{Ir}]^+ \rightarrow [\mathrm{Ir}]^{2+\bullet} + [\mathrm{Ir}]^\bullet$$

$$\text{b. } {}^3[\mathrm{Ir}]^+ + {}^3[\mathrm{Ir}]^+ \rightarrow [\mathrm{Ir}]^{2+\bullet} + [\mathrm{Ir}]^\bullet$$

To establish the occurrence of these processes, vertical electron affinity (VEA) and ionization potential (VIP) of the PS in its ground and triplet excited states have been determined for both the complexes and are summarized in Table 2, together with the VEA of molecular oxygen computed at the same level of theory. Data reported, again, evidence the same propensity of the prodrug **Ir-B(OH)$_2$** and the active PS **Ir-OH** to lose and gain electrons. According to pathway a, the PS in the triplet state transfers an electron to a neighbouring molecule of PS in the ground state, thus the sum of the ground state VIP and triplet state VEA should be less than zero. For pathway b to occur, instead, as the electron transfer occurs between two neighbouring molecules of PS in the triplet state $^3[\mathrm{Ir}]^+$, the sum of VEA and VIP of triplet state should lead to the same result. Accordingly, while autoionization reaction b can be favourable, pathway a is not viable in both the complexes.

Table 2 VEA and VIP values (eV) computed in water for $^3O_2$[a] and Ir(III) complexes, **Ir-B(OH)$_2$** and **Ir-OH**, in their ground and triplet excited states

	$[\mathrm{Ir}]^+$		$^3[\mathrm{Ir}]^+$	
	VEA	VIP	VEA	VIP
Ir-B(OH)$_2$	−2.74	5.80	−5.36	3.17
Ir-OH	−2.74	5.80	−5.37	3.17

[a] VEA O_2 = −2.33 eV computed at the PBE0/6-311G* level.

As stated above, the PS in the triplet state can transfer an electron to the molecular oxygen directly affording $O_2^{-\bullet}$, or transfer the electron only after triplet state reduction to the species $[\mathrm{Ir}]^\bullet$ obtained following the autoionization reactions just described. The two reactions can be summarized as:

$$\text{c. } {}^3[\mathrm{Ir}]^+ + {}^3O_2 \rightarrow [\mathrm{Ir}]^{2+\bullet} + O_2{}^{(-)\bullet}$$

$$\text{d. } [\mathrm{Ir}]^\bullet + {}^3O_2 \rightarrow [\mathrm{Ir}]^+ + O_2{}^{(-)\bullet}$$

To establish whether the two complexes can directly transfer an electron to $^3O_2$, the condition that the sum of oxygen VEA and $^3[\mathrm{Ir}]^+$ VIP is negative should be verified. Being VIPs computed for the two complexes in the triplet state higher than the absolute value of oxygen VEA, pathway c becomes inaccessible to both the Ir(III) complexes herein considered. Similarly, for verifying the occurrence of pathway d, that follows the $[\mathrm{Ir}]^\bullet$ formation according to the favourable pathway b, the sum of the oxygen VEA and VIP of [Ir]˙ should be less than zero. Even this process is not feasible; hence the Ir(III) complexes here investigated cannot trigger type I photoreactions but can act only as $^1O_2$ generators according to type II reactions.

Conclusions

In this work, a DFT-based theoretical investigation has been performed to clarify the mechanism of action of a recently synthesized Ir(III) charged complex, **Ir-B(OH)$_2$**. The complex is characterized by the presence of an aryl boronic acid moiety on one of the three bidentate ligands, which can be exploited to detect H_2O_2 in cancer cells. The H_2O_2-mediated oxidation of boronic acids under physiological conditions affords the active complex for PDT application, **Ir-OH**, and QM as a by-product, which in turn can scavenge GSH compromising one of the most powerful cellular defence against the ROS produced by PDT treatments. The most plausible reaction mechanism for the oxidation of the aryl boronic acid by H_2O_2 has been explored by considering the intervention of both H_2O_2 and HOO^- species, and the H_2O_2-responsive part of the complex, the aryl boronic acid. The reaction mechanism involving the neutral species requires the intervention of at least two water molecules that are directly involved in the process and extra molecules that have to assist the steps involving proton transfer. However, the action of anion species is easier to occur requiring essentially only the involvement of the water molecules needed as reactants. The energies put into play suggest that a neutral reaction could occur overcoming an energy barrier of 33 kcal mol^{-1}, which accounts for the H_2O_2 nucleophile attack to the boron atom (RDS). In contrast, the anion attack is much favoured from a kinetic point of view and the RDS (15.3 kcal mol^{-1}) is represented by the final cleavage of the C–O bond in favour of the product release. The formation of the products, namely the PS **Ir-OH** and the QM, is achieved with a considerable energy gain following both the pathways. Though the products along the anion pathway are slightly less stable, the kinetics is strongly in favour of HOO^- involvement in the oxidation reaction. The description of the subsequent GSH scavenging by the released QM evidences that the reaction occurs with a low energy expense, 12.7 kcal mol^{-1} being the energy barrier that has to be overcome for the phenol–SG adduct formation. In addition, the exploration of the photophysical properties suggests that both the prodrug **Ir-B(OH)$_2$** and the active PS **Ir-OH** are able to generate the most harmful cytotoxic agent in PDT, $^1O_2$, according to type II photoreactions, while type I reactions are inaccessible to both the complexes. Outcomes of such exploration unravel that the metal centre takes part in the charge density of the molecular orbitals characterizing the excited states and, accordingly, promotes ISC needed to populate a triplet state, the PS's state deputed to the energy transfer to molecular oxygen.

These findings clearly show that the prodrug **Ir-B(OH)$_2$** can exert synergistic anticancer effects in the presence of H_2O_2 from sequential actions of the GSH-scavenger QM and ROS generating **Ir-OH** and can stimulate the design of more and more efficient Ir(III)-based photosensitizers.

Computational details

All the quantum mechanical calculations, based on density functional theory, have been performed using the Gaussian 16 package.[54] To simulate the physiological environment, all the calculations have been carried out within the water medium (ε = 78.4). Solvation effects have been included using the PCM continuum model.[55,56] The standard triplet ζ basis set 6-311G (d,p) has been employed for all the atoms with the exception of oxygen and sulphur atoms, for which a diffuse function has been added, and the metal, which is described by the SDD effective core potential[57] and the corresponding valence basis set. All the minima and transition states have been optimized employing the hybrid functional B3LYP,[58,59] and dispersive interaction have been explained through Grimme's empirical correction (GD3).[60] To confirm the nature of all the optimized structures, harmonic vibrational frequency calculations have been performed, and zero and one imaginary frequency have been checked for minima and transition states, respectively. For each identified transition state (TS), intrinsic reaction coordinate (IRC) calculations have been performed to properly identify reagents and products of each reaction step. Furthermore, these calculations, resulted by the inspection of the transition states involving H-transfer, have been used to estimate the tunnelling effect according to the approximate Wigner formula.[61] A tunnelling correction ranking from 4 to 12 has been obtained for such steps, similar to other systems.[62–66]

For an accurate description of the photophysical properties, a preliminary benchmark study has been conducted on the maximum absorption wavelength of the complex **Ir-OH**. For this purpose, time dependent (TD-DFT) calculations on the B3LYP-D3 optimized structure have been performed using different exchange–correlation functionals: B3PW91,[67] B97D,[68] CAM-B3LYP,[69] LC-WHPBE,[70] M06,[71] M06L,[72] M11,[73] MN15,[74] PBE0,[75] WB97XD,[76] PBE,[77,78] MN15L,[79] MN12L,[80] N12,[81] M08-HX[82] and TPSS.[83] The result of the benchmark study returns the hybrid functionals MN15 and PBE0 as the most suitable in confirming one of the main properties for PDT application, $\lambda_{\max}$. However, due to the need to use another software, ORCA package,[84] for computing other photophysical parameters described below, PBE0 is selected as it is the only available in such software; thus, it is used for computing all the photophysical properties of the Ir(III) complexes under investigation.

To confirm the possibility of an intersystem spin crossing between singlet and triplet excited states, spin–orbit matrix elements have been computed using the SOC-TD-DFT approach implemented in the ORCA package.[84] Relativistic corrections have been computed by the zeroth order regular approximation (ZORA) on the ground state optimized geometry eploying PBE0 functional. ZORA-DEF2-SVP and SARC-ZORA-SVP basis sets for the main and metal atoms have been employed, respectively. The spin–orbit coupling values (SOCs) have been, thus calculated as previously reported, as the square root of the square modulus of the matrix elements:[85–87]

$$\mathrm{SOC}_{mn} = \sqrt{\sum_i \left| \left\langle \psi_{\mathrm{S}_m} \middle| \hat{H}_{\mathrm{SO}} \middle| \psi_{\mathrm{T}_{i,n}} \right\rangle \right|^2};\ i = x, y, z \qquad (2)$$

where H_{SO} is the mean-field/effective potentials operator, including one-electron terms with the RI-SOMF(1X) option chosen to accelerate the SOC integrals calculation.[88]

To establish the occurring of type 1 photodynamic processes, vertical ionization potential (VIP) and vertical electron affinity (VEA) have been computed for both ground and excited triplet states of the two considered Ir(III) complexes using the same level of theory employed for the computation of other photophysical properties.

Author contributions

The manuscript was written through contributions of all the authors. All the authors have given approval to the final version of the manuscript.

Conflicts of interest

There are no conflicts to declare.

Acknowledgements

This research was supported by the University of Calabria. The authors gratefully acknowledge the computing time granted by the CINECA (project IsCa3_MoAMCPCT).

References

1 J. F. Lovell, T. W. B. Liu, J. Chen and G. Zheng, Activatable Photosensitizers for Imaging and Therapy, *Chem. Rev.*, 2010, **110**, 2839–2857.

2 E. J. G. Dennis, J. Dolmans, D. Fukumura and R. K. Jain, Photodynamic therapy for cancer, *Nat. Rev. Cancer*, 2003, **3**, 380–387.

3 P. Agostinis, K. Berg, K. A. Cengel, T. H. Foster, A. W. Girotti, S. O. Gollnick, S. M. Hahn, M. R. Hamblin, A. Juzeniene, D. Kessel, M. Korbelik, J. Moan, P. Mroz, D. Nowis, J. Piette, B. C. Wilson and J. Golab, Photodynamic therapy of cancer: An update, *CA Cancer J. Clin.*, 2011, **61**, 250–281.

4 J. D. Bhawalkar, N. D. Kumar, C. F. Zhao and P. N. Prasad, Two-photon photodynamic therapy, *J. Clin. Laser Med. Surg.*, 1997, **15**, 201–204.

5 R. R. Allison and K. Moghissi, Photodynamic Therapy (PDT): PDT Mechanisms, *Clin. Endosc.*, 2013, **46**, 24–29.

6 S. S. Sabharwal and P. T. Schumacker, Mitochondrial ROS in cancer: initiators, amplifiers or an Achilles' heel?, *Nat. Rev. Cancer*, 2014, **14**, 709–721.

7 S. W. G. Tait and D. R. Green, Mitochondria and cell death: outer membrane permeabilization and beyond, *Nat. Rev. Mol. Cell Biol.*, 2010, **11**, 621–632.

8 S. Fulda, L. Galluzzi and G. Kroemer, Targeting mitochondria for cancer therapy, *Nat. Rev. Drug Discovery*, 2010, **9**, 447–464.

9 X. Liao, J. Shen, W. Wu, S. Kuang, M. Lin, J. Karges, Z. Tang and H. Chao, A mitochondrial-targeting iridium (III) complex for H_2O_2-responsive and oxidative stress amplified two-photon photodynamic therapy, *Inorg. Chem. Front.*, 2021, **8**, 5045–5053.

10 S. Bonnet, Shifting the Light Activation of Metallodrugs to the Red and Near-Infrared Region in Anticancer Phototherapy, *Comments Inorg. Chem.*, 2015, **35**, 179–213.

11 F. Heinemann, J. Karges and G. Gasser, Critical Overview of the Use of Ru(II) Polypyridyl Complexes as Photosensitizers in One-Photon and Two-Photon Photodynamic Therapy, *Acc. Chem. Res.*, 2017, **50**, 2727–2736.

12 F. Reeßing and W. Szymanski, *Beyond Photodynamic Therapy: Light-Activated Cancer Chemotherapy*, Bentham Science Publishers, 2018, vol. 24.

13 J. Liu, C. Zhang, T. W. Rees, L. Ke, L. Ji and H. Chao, Harnessing ruthenium(II) as photodynamic agents: Encouraging advances in cancer therapy, *Coord. Chem. Rev.*, 2018, **363**, 17–28.

14 F. E. Poynton, S. A. Bright, S. Blasco, D. C. Williams, J. M. Kelly and T. Gunnlaugsson, The development of ruthenium(II) polypyridyl complexes and conjugates for in vitro cellular and in vivo applications, *Chem. Soc. Rev.*, 2017, **46**, 7706–7756.

15 J. D. Knoll, B. A. Albani and C. Turro, Excited state investigation of a new Ru(II) complex for dual reactivity with low energy light, *Chem. Commun.*, 2015, **51**, 8777–8780.

16 J. K. White, R. H. Schmehl and C. Turro, An overview of photosubstitution reactions of Ru(II) imine complexes and their application in photobiology and photodynamic therapy, *Inorg. Chim. Acta*, 2017, **454**, 7–20.

17 N. A. Smith and P. J. Sadler, Photoactivatable metal complexes: from theory to applications in biotechnology and medicine, *Philos. Trans. R. Soc., A*, 2013, **371**, 20120519.

18 A. Zamora, G. Vigueras, V. Rodríguez, M. D. Santana and J. Ruiz, Cyclometalated iridium(III) luminescent complexes in therapy and phototherapy, *Coord. Chem. Rev.*, 2018, **360**, 34–76.

19 X. Jiang, N. Zhu, D. Zhao and Y. Ma, New cyclometalated transition-metal based photosensitizers for singlet oxygen generation and photodynamic therapy, *Sci. China: Chem.*, 2016, **59**, 40–52.

20 S. Lazic, P. Kaspler, G. Shi, S. Monro, T. Sainuddin, S. Forward, K. Kasimova, R. Hennigar, A. Mandel, S. McFarland and L. Lilge, Novel Osmium-based Coordination Complexes as Photosensitizers for Panchromatic Photodynamic Therapy, *Photochem. Photobiol.*, 2017, **93**, 1248–1258.

21 J. J. Cao, C. P. Tan, M. H. Chen, N. Wu, D. Y. Yao, X. G. Liu, L. N. Ji and Z. W. Mao, Targeting cancer cell metabolism with mitochondria-immobilized phosphorescent cyclometalated iridium(III) complexes, *Chem. Sci.*, 2016, **8**, 631–640.

22 W. Lv, Z. Zhang, K. Y. Zhang, H. Yang, S. Liu, A. Xu, S. Guo, Q. Zhao and W. Huang, A Mitochondria-Targeted Photosensitizer Showing Improved Photodynamic Therapy Effects Under Hypoxia, *Angew. Chem., Int. Ed.*, 2016, **55**, 9947–9951.

23 L. He, M. F. Zhang, Z. Y. Pan, K. N. Wang, Z. J. Zhao, Y. Li and Z. W. Mao, A mitochondria-targeted iridium(III)-based photoacid generator induces dual-mode photodynamic damage within cancer cells, *Chem. Commun.*, 2019, **55**, 10472–10475.

24 K. V. Sudheesh, P. S. Jayaram, A. Samanta, K. S. Bejoymohandas, R. S. Jayasree and A. Ajayaghosh, A Cyclometalated IrIII Complex as a Lysosome-Targeted Photodynamic Therapeutic Agent for Integrated Imaging and Therapy in Cancer Cells, *Chem. – Eur. J.*, 2018, **24**, 10999–11007.

25 S. Toyokuni, K. Okamoto, J. Yodoi and H. Hiai, Persistent oxidative stress in cancer, *FEBS Lett.*, 1995, **358**, 1–3.

26 E. O. Hileman, J. Liu, M. Albitar, M. J. Keating and P. Huang, Intrinsic oxidative stress in cancer cells: a biochemical basis for therapeutic selectivity, *Cancer Chemother. Pharmacol.*, 2004, **53**, 209–219.

27 D. Kang and N. Hamasaki, Mitochondrial oxidative stress and mitochondrial DNA, *Clin. Chem. Lab. Med.*, 2003, **41**, 1281–1288.

28 L. Behrend, G. Henderson and R. M. Zwacka, Reactive oxygen species in oncogenic transformation, *Biochem. Soc. Trans.*, 2003, **31**, 1441–1444.

29 F. Q. Schafer and G. R. Buettner, Redox environment of the cell as viewed through the redox state of the glutathione disulfide/glutathione couple, *Free Radicals Biol. Med.*, 2001, **30**, 1191–1212.

30 Q. Zeng, R. Zhang, T. Zhang and D. Xing, H_2O_2-responsive biodegradable nanomedicine for cancer-selective dual-modal imaging guided precise photodynamic therapy, *Biomaterials*, 2019, **207**, 39–48.

31 C. Mytilineou, B. C. Kramer and J. A. Yabut, Glutathione depletion and oxidative stress, *Parkinsonism Relat. Disord.*, 2002, **8**, 385–387.

32 Q. Pan, B. Zhang, X. Peng, S. Wan, K. Luo, W. Gao, Y. Pu and B. He, A dithiocarbamate-based H_2O_2-responsive prodrug for combinational chemotherapy and oxidative stress amplification therapy, *Chem. Commun.*, 2019, **55**, 13896–13899.

33 C. C. Song, F. S. Du and Z. C. Li, Oxidation-responsive polymers for biomedical applications, *J. Mater. Chem. B*, 2014, **2**, 3413–3426.

34 Y. Xu, W. Shi, H. Li, X. Li and H. Ma, H_2O_2-Responsive Organosilica-Doxorubicin Nanoparticles for Targeted Imaging and Killing of Cancer Cells Based on a Synthesized Silane-Borate Precursor, *ChemMedChem*, 2019, **14**, 1079–1085.

35 Y. Hu, X. Li, Y. Fang, W. Shi, X. Li, W. Chen, M. Xian and H. Ma, Reactive oxygen species-triggered off-on fluorescence donor for imaging hydrogen sulfide delivery in living cells, *Chem. Sci.*, 2019, **10**, 7690–7694.

36 B. Gatin-Fraudet, R. Ottenwelter, T. Le Saux, S. Norsikian, M. Pucher, T. Lombès, A. Baron, P. Durand, G. Doisneau, Y. Bourdreux, B. I. Iorga, M. Erard, L. Jullien, D. Guianvarc'h, D. Urban and B. Vauzeilles, Evaluation of borinic acids as new, fast hydrogen peroxide–responsive triggers, *Proc. Natl. Acad. Sci. U. S. A.*, 2021, **118**, e2107503118.

37 X. Liao, J. Shen, W. Wu, S. Kuang, M. Lin, J. Karges, Z. Tang and H. Chao, A mitochondrial-targeting iridium (III) complex for H_2O_2-responsive and oxidative stress amplified two-photon photodynamic therapy, *Inorg. Chem. Front.*, 2021, **8**, 5045–5053.

38 J. Noh, B. Kwon, E. Han, M. Park, W. Yang, W. Cho, W. Yoo, G. Khang and D. Lee, Amplification of oxidative stress by a dual stimuli-responsive hybrid drug enhances cancer cell death, *Nat. Commun.*, 2015, **6**, 1–9.

39 J. Li, A. Dirisala, Z. Ge, Y. Wang, W. Yin, W. Ke, K. Toh, J. Xie, Y. Matsumoto, Y. Anraku, K. Osada and K. Kataoka, Therapeutic Vesicular Nanoreactors with Tumor-Specific Activation and Self-Destruction for Synergistic Tumor Ablation, *Angew. Chem.*, 2017, **129**, 14213–14218.

40 A. R. Lippert, G. C. Van De Bittner and C. J. Chang, Boronate oxidation as a bioorthogonal reaction approach for studying the chemistry of hydrogen peroxide in living systems, *Acc. Chem. Res.*, 2011, **44**, 793–804.

41 H. Kikuchi, Y. Nakamura, C. Inoue, S. Nojiri, M. Koita, M. Kojima, H. Koyama, R. Miki, T. Seki and Y. Egawa, Hydrogen Peroxide-Triggered Conversion of Boronic Acid-Appended Insulin into Insulin and Its Application as a Glucose-Responsive Insulin Formulation, *Mol. Pharm.*, 2021, **18**, 4224–4230.

42 N. Agmon, The Grotthuss mechanism, *Chem. Phys. Lett.*, 1995, **244**, 456–462.

43 F. Ponte, G. Mazzone, N. Russo and E. Sicilia, Activation by Glutathione in Hypoxic Environment of an Azo-based Rhodamine Activatable Photosensitizer. A Computational Elucidation, *Chem. – Eur. J.*, 2022, **28**, e202104083.

44 D. N. R. Rao, N. Takahashi and R. P. Mason, Characterization of a glutathione conjugate of the 1,4-benzosemiquinone-free radical formed in rat hepatocytes., *J. Biol. Chem.*, 1988, **263**, 17981–17986.

45 A. R. Amaro, G. G. Oakley, U. Bauer, H. P. Spielmann and L. W. Robertson, Metabolic activation of PCBs to quinones: Reactivity toward nitrogen and sulfur nucleophiles and influence of superoxide dismutase, *Chem. Res. Toxicol.*, 1996, **9**, 623–629.

46 N. Hulsman, J. P. Medema, C. Bos, A. Jongejan, R. Leurs, M. J. Smit, I. J. P. De Esch, D. Richel and M. Wijtmans, Chemical insights in the concept of hybrid drugs: The antitumor effect of nitric oxide-donating aspirin involves a quinone methide but not nitric oxide nor aspirin, *J. Med. Chem.*, 2007, **50**, 2424–2431.

47 H. Hagen, P. Marzenell, E. Jentzsch, F. Wenz, M. R. Veldwijk and A. Mokhir, Aminoferrocene-based prodrugs activated by reactive oxygen species, *J. Med. Chem.*, 2012, **55**, 924–934.

48 J. P. Cerón-Carrasco, J. Ruiz, C. Vicente, C. de Haro, D. Bautista, J. Zúñiga and A. Requena, DFT Simulation of Structural and Optical Properties of 9-Aminoacridine Half-Sandwich Ru(II), Rh(III), and Ir(III) Antitumoral Complexes and Their Interaction with DNA, *J. Chem. Theory Comput.*, 2017, **13**, 3898–3910.

49 G. Mazzone, M. E. Alberto, N. Russo and E. Sicilia, Ab initio calculations on the 1O2 quenching mechanism by trans-resveratrol, *Phys. Chem. Chem. Phys.*, 2014, **16**, 12773–12781.

50 M. E. Alberto, B. C. De Simone, G. Mazzone, E. Sicilia and N. Russo, The heavy atom effect on Zn(II) phthalocyanine derivatives: A theoretical exploration of the photophysical properties, *Phys. Chem. Chem. Phys.*, 2015, **17**, 23595–23601.

51 G. Mazzone, M. Alberto, B. De Simone, T. Marino and N. Russo, Can Expanded Bacteriochlorins Act as Photosensitizers in Photodynamic Therapy? Good News from Density Functional Theory Computations, *Molecules*, 2016, **21**, 288.

52 V. Butera, G. Mazzone and H. Detz, Dinuclear Ruthenium (II)-Pyrrolide Complexes Linked by Different Organic Units as PDT Photosensitizers: Computational Study of the Linker Influence on the Photophysical Properties*, *ChemPhotoChem*, 2022, **6**, e202200094.

53 L. Skripnikov, *Chemissian 4.67*, **https://www.chemissian.com/**.

54 M. J. Frisch, G. W. Trucks, H. B. Schlegel, G. E. Scuseria, M. A. Robb, J. R. Cheeseman, G. Scalmani, V. Barone, G. A. Petersson, H. Nakatsuji, X. Li, M. Caricato, a. V. Marenich, J. Bloino, B. G. Janesko, R. Gomperts, B. Mennucci, H. P. Hratchian, J. V. Ortiz, A. F. Izmaylov, J. L. Sonnenberg, D. Williams-Young, F. Ding, F. Lipparini, F. Egidi, J. Goings, B. Peng, A. Petrone, T. Henderson, D. Ranasinghe, V. G. Zakrzewski, J. Gao, N. Rega, G. Zheng, W. Liang, M. Hada, M. Ehara, K. Toyota, R. Fukuda, J. Hasegawa, M. Ishida, T. Nakajima, Y. Honda, O. Kitao, H. Nakai, T. Vreven, K. Throssell, J. A. Montgomery Jr., J. E. Peralta, F. Ogliaro, M. J. Bearpark, J. J. Heyd, E. N. Brothers, K. N. Kudin, V. N. Staroverov, T. A. Keith, R. Kobayashi, J. Normand, K. Raghavachari, A. P. Rendell, J. C. Burant, S. S. Iyengar, J. Tomasi, M. Cossi, J. M. Millam, M. Klene, C. Adamo, R. Cammi, J. W. Ochterski, R. L. Martin, K. Morokuma, O. Farkas, J. B. Foresman and D. J. Fox, *Gaussian 16, Revision C.01*, Gaussian, Inc., Wallin, 2016.

55 S. Miertuš, E. Scrocco and J. Tomasi, Electrostatic interaction of a solute with a continuum. A direct utilizaion of AB initio molecular potentials for the prevision of solvent effects, *Chem. Phys.*, 1981, **55**, 117–129.

56 S. Miertuš and J. Tomasi, Approximate evaluations of the electrostatic free energy and internal energy changes in solution processes, *Chem. Phys.*, 1982, **65**, 239–245.

57 D. Andrae, U. Häußermann, M. Dolg, H. Stoll and H. Preuß, Energy-adjustedab initio pseudopotentials for the second and third row transition elements, *Theor. Chim. Acta*, 1990, **77**, 123–141.

58 A. D. Becke, Density–functional thermochemistry. III. The role of exact exchange, *J. Chem. Phys.*, 1998, **98**, 5648.

59 C. Lee, W. Yang and R. G. Parr, Development of the Colle-Salvetti correlation-energy formula into a functional of the electron density, *Phys. Rev. B: Condens. Matter Mater. Phys.*, 1988, **37**, 785.

60 S. Grimme, Semiempirical GGA-type density functional constructed with a long-range dispersion correction, *J. Comput. Chem.*, 2006, **27**, 1787–1799.

61 E. Wigner, On the Quantum Correction For Thermodynamic Equilibrium, *Phys. Rev.*, 1932, **40**, 749–759.

62 W. R. Schulz and D. J. Le Roy, Kinetics of the Reaction H + p–H_2 = o–H_2 + H, *J. Chem. Phys.*, 1965, **42**, 3869–3873.

63 Y. Zhang, J. B. Rommel, M. T. Cvitaš and S. C. Althorpe, Shallow-tunnelling correction factor for use with Wigner–Eyring transition-state theory, *Phys. Chem. Chem. Phys.*, 2014, **16**, 24292–24300.

64 N. Tanaka, S. Itoh and H. Nishikiori, Density functional theory studies on the addition and abstraction reactions of OH radicals with terephthalate dianions, *Int. J. Quantum Chem.*, 2013, **113**, 418–422.

65 W. H. Miller, S. D. Schwartz and J. W. Tromp, Quantum mechanical rate constants for bimolecular reactions, *J. Chem. Phys.*, 1983, **79**, 4889–4898.

66 B. C. Garrett, D. G. Truhlar, J. M. Bowman, A. F. Wagner, D. Robie, S. Arepalli, N. Presser and R. J. Gordon, Ab Initio Predictions and Experimental Confirmation of Large Tunneling Contributions to Rate Constants and Kinetic Isotope Effects for Hydrogen Atom Transfer Reactions, *J. Am. Chem. Soc.*, 1986, **108**, 3515–3516.

67 J. P. Perdew and K. Burke, Generalized gradient approximation for the exchange-correlation hole of a many-electron system, *Phys. Rev. B: Condens. Matter Mater. Phys.*, 1996, **54**, 16533.

68 S. Grimme, Semiempirical hybrid density functional with perturbative second-order correlation, *J. Chem. Phys.*, 2006, **124**, 034108.

69 T. Yanai, D. P. Tew and N. C. Handy, A new hybrid exchange–correlation functional using the Coulomb-attenuating method (CAM-B3LYP), *Chem. Phys. Lett.*, 2004, **393**, 51–57.

70 O. A. Vydrov and G. E. Scuseria, Assessment of a long-range corrected hybrid functional, *J. Chem. Phys.*, 2006, **125**, 234109.

71 Y. Zhao and D. G. Truhlar, The M06 suite of density functionals for main group thermochemistry, thermochemical kinetics, noncovalent interactions, excited states, and transition elements: two new functionals and systematic testing of four M06-class functionals and 12 other function, *Theor. Chem. Acc.*, 2008, **120**, 215–241.

72 Y. Zhao and D. G. Truhlar, A new local density functional for main-group thermochemistry, transition metal bonding, thermochemical kinetics, and noncovalent interactions, *J. Chem. Phys.*, 2006, **125**, 194101.

73 R. Peverati and D. G. Truhlar, Improving the accuracy of hybrid meta-GGA density functionals by range separation, *J. Phys. Chem. Lett.*, 2011, **2**, 2810–2817.

74 H. S. Yu, X. He, S. L. Li and D. G. Truhlar, MN15: A Kohn–Sham global-hybrid exchange–correlation density functional with broad accuracy for multi-reference and single-reference systems and noncovalent interactions, *Chem. Sci.*, 2016, **7**, 5032.

75 C. Adamo and V. Barone, Toward reliable density functional methods without adjustable parameters: The PBE0 model, *J. Chem. Phys.*, 1999, **110**, 6158.

76 J. Da Chai and M. Head-Gordon, Long-range corrected hybrid density functionals with damped atom–atom dispersion corrections, *Phys. Chem. Chem. Phys.*, 2008, **10**, 6615–6620.

77 J. P. Perdew, K. Burke and M. Ernzerhof, Generalized Gradient Approximation Made Simple, *Phys. Rev. Lett.*, 1996, **77**, 3865.

78 J. P. Perdew, K. Burke and M. Ernzerhof, Generalized Gradient Approximation Made Simple [Phys. Rev. Lett. 77, 3865 (1996)], *Phys. Rev. Lett.*, 1997, **78**, 1396.

79 H. S. Yu, X. He and D. G. Truhlar, MN15-L: A New Local Exchange-Correlation Functional for Kohn-Sham Density Functional Theory with Broad Accuracy for Atoms, Molecules, and Solids, *J. Chem. Theory Comput.*, 2016, **12**, 1280–1293.

80 R. Peverati and D. G. Truhlar, An improved and broadly accurate local approximation to the exchange–correlation density functional: The MN12-L functional for electronic structure calculations in chemistry and physics, *Phys. Chem. Chem. Phys.*, 2012, **14**, 13171–13174.

81 R. Peverati and D. G. Truhlar, Exchange-correlation functional with good accuracy for both structural and energetic properties while depending only on the density and its gradient, *J. Chem. Theory Comput.*, 2012, **8**, 2310–2319.

82 Y. Zhao and D. G. Truhlar, Exploring the limit of accuracy of the global hybrid meta density functional for main-group thermochemistry, kinetics, and noncovalent interactions, *J. Chem. Theory Comput.*, 2008, **4**, 1849–1868.

83 J. Tao, J. P. Perdew, V. N. Staroverov and G. E. Scuseria, Climbing the density functional ladder: Nonempirical meta–generalized gradient approximation designed for molecules and solids, *Phys. Rev. Lett.*, 2003, **91**, 146401.

84 F. Neese and J. Wiley, The ORCA program system, *Wiley Interdiscip. Rev.: Comput. Mol. Sci.*, 2012, **2**, 73–78.

85 S. Scoditti, E. Dabbish, N. Russo, G. Mazzone and E. Sicilia, Anticancer Activity, DNA Binding, and Photodynamic Properties of a N^C^N-Coordinated Pt(II) Complex, *Inorg. Chem.*, 2021, **60**, 10350–10360.

86 E. Dabbish, G. Mazzone, N. Russo and E. Sicilia, Mechanism of action of the curcumin cis-diammineplatinum(II) complex as a photocytotoxic agent, *Inorg. Chem. Front.*, 2020, **7**, 2759–2769.

87 S. Scoditti, G. Mazzone, N. Sanna and E. Sicilia, Computational Exploration of the Synergistic Anticancer Effect of a Multi-Action Ru(II)–Pt(IV) Conjugate, *Inorg. Chem.*, 2022, **61**, 12903–12912.

88 F. Neese, Efficient and accurate approximations to the molecular spin-orbit coupling operator and their use in molecular g-tensor calculations, *J. Chem. Phys.*, 2005, **122**, 034107.